

3D printed human skull phantoms for transcranial photoacoustic imaging

Hannah Linde¹, Saskia Menzer¹, Jan Laufer¹, Thomas Kirchner^{1*}

¹ Institut für Physik, Martin-Luther-Universität Halle-Wittenberg, Halle (Saale), Germany

* thomas.kirchner@physik.uni-halle.de

Abstract: Photoacoustic (PA) waves are strongly distorted and attenuated in skull bone. To study these effects on PA imaging, we designed and 3D-printed tissue-mimicking phantoms of human skull. We present a comparison of results in phantom and *ex vivo* skull.

1. Introduction

Photoacoustic (PA) brain imaging has the potential to be translated into a real-time non-ionizing clinical modality which could provide faster diagnosis and monitoring for time-critical brain injuries, compared to slower current clinical imaging modalities like X-ray computer tomography (CT) and magnetic resonance imaging (MRI). [1] Applications of PA measurements of the human brain through the intact skin and skull could include monitoring of brain hemodynamics, the detection of intracranial bleeding, and supporting stroke diagnosis [1, 2].

The strong acoustic attenuation and wavefront distortion introduced by cranial bone tissue pose significant challenges for biomedical photoacoustic imaging [3,4] as they result in reduced image resolution and contrast [5]. In previous work [6], tissue-mimicking human bone phantoms were fabricated using a combination of fused deposition modelling (FDM) and stereolithography (SLA), producing SLA resin-printed temporal bone phantoms for PAI. That work suggested that materials used in FDM printing are not sufficiently transmissive to ultrasound. High acoustic attenuation is actually desirable in skull phantoms as ultrasound above approximately 2MHz does not penetrate thick human skull [7]. A disadvantage of SLA 3D printing is its inability to create hollow structures, such as the diploë pores in thick skull bone, without drainage holes [8]. Another approach to mimicking skull in experiments is the use of a spherical acrylic shell as a skull phantom [9]. Acrylic is an elastic solid that possesses acoustic properties similar to bone but it lacks the micro-structure of the diploë and therefore does not match the acoustic aberration of thick skull.

In this work, we developed a skull-mimicking phantom using FDM 3D printing, which allows us to fabricate a water-permeable, porous medium. As FDM 3D printing allows for rapid prototyping, we iteratively optimized printing parameters, resulting in a printed phantom of a human frontal cranial bone which has acoustic properties closely mimicking tissue.

2. Materials and methods

We created a printable mesh model of a representative right frontal cranial bone based on a bone segmentation obtained from an X-ray micro-CT data set [10]. The corresponding skull bone of a 70-year-old male body donor was used as the reference for our printed frontal bone phantoms. Thick skull bone, like the frontal cranial bone (general thickness of 6 to 9 mm), is composed of an outer and an inner layer of solid cortical bone separated by a cancellous bone layer – the diploë – which accounts for $(54 \pm 15) \%$ of the skull thickness [11].

We generated the mesh from the bone segmentation using the Medical Imaging Interaction Toolkit (MITK) [12]. We limited the mesh size due to computational constraints by reducing the mesh vertices to 25% without any relevant loss in detail. Example sections of a micro-CT slice and the corresponding bone segmentation are shown in Figure 1a. A section of one slice of the resulting print path is shown in Figure 1b. 15 phantom versions were printed based on this mesh (see Data availability) with varying printing parameters. Acoustic transmission measurements and PA imaging were performed through the resulting 3D-printed phantoms and the corresponding *ex vivo* skull.

3D printing of skull phantoms

The phantoms were printed with Polylactide (PLA) filament, the most widely used 3D printing filament. We printed the phantoms with varying resolution (printing nozzle size and layer height) and porosity (by artificially enlarging the diploë pores). For the latter we used the *hole compensation* method in the slicing software. To mimic solid cortical bone, the infill density was generally set to 100%. Full print settings can be found in the Data availability section. The phantom print paths were prepared using a slicing software (Bambu Studio, Bambu Lab, Shenzhen, China) and printed using a widely used printer (Bambu X1 Carbon, Bambu Lab, Shenzhen, China).

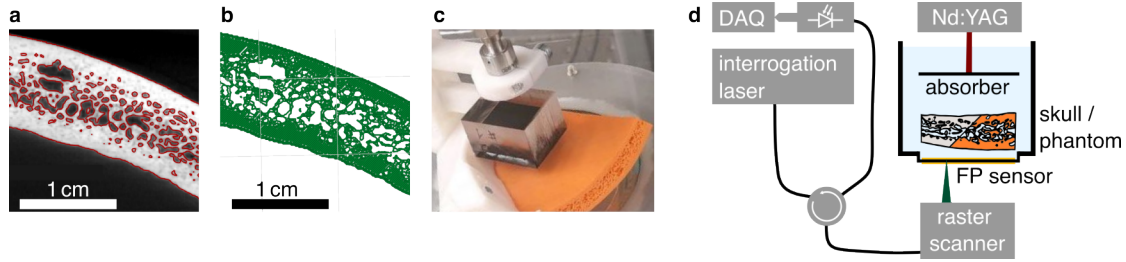


Fig. 1. **a** example slice of the micro-CT with bone segmentation boundary in red, **b** print path for the same slice, **c** resulting printed phantom (orange) during characterization. **d** Transmission measurement setup. PA imaging through *ex vivo* human skull and skull phantoms. The planar PA source, a black-coated acrylic glass block, is illuminated by an Nd:YAG excitation laser and generates PA wavefronts. These propagate through a region of frontal cranial bone or phantom and are measured by a planar Fabry-Perot (FP) sensor, raster-scanned by an interrogation laser.

The phantoms were printed with varying formulations of PLA: PLA Basic, PLA Matte or PLA Tough (Bambu Lab, Shenzhen, China). Table 1 compares the mechanical properties of PLA (as provided by the manufacturer) to cranial bone. The speed of sound was measured by ultrasound transmission through massive printed PLA slabs.

Table 1. Mechanical properties of human skull bone [13–15] compared to PLA filament

	Cranial bone	PLA
Density [g/cm^3]	1.71 ± 0.13	1.27 ± 0.03
Elastic modulus [GPa]	3.81 ± 1.55	2.38 ± 0.36
Tensile strength [MPa]	67.73 ± 17.8	33.67 ± 7.36
Bending modulus [GPa]	11.73 ± 0.95	2.68 ± 0.35
Bending strength [MPa]	82.0 ± 25.5	72 ± 9.99
Speed of sound [m/s]	2504 ± 120	2115 ± 4

Photoacoustic transmission measurements and imaging

As illustrated in Figure 1d, a layer of black acrylic paint on a PMMA substrate is used as a PA source. The emitted PA wavefronts are measured after passing through either *ex vivo* human skull or the printed phantoms.

We used a Fabry-Perot (FP) raster scanning tomograph setup for single point measurements and PA imaging. The scanner is based on Zhang *et al.* [16] and incorporates a broadband planar FP sensor as described by Buchmann *et al.* [17]. We compare the acoustic power spectra of the insertion losses in the samples (skull phantoms, *ex vivo* human skull). A Nd:YAG excitation laser (Quanta-Ray PRO-270-50H, Spectra-Physics Lasers, Santa Clara, USA) was used for PA excitation at 1064 nm with pulse durations of ~ 10 ns and a pulse repetition rate of 50 Hz. Tomographic data sets were acquired by raster scanning the interrogation beam across a detection aperture of $1.6\text{ cm} \times 1.6\text{ cm}$ in 0.1 mm steps using galvanometer mirrors (GVS012, Thorlabs) and recording the time-resolved PA signals at each position.

To avoid air inclusions, the water tank was filled with degassed and deionized water in which the samples were submerged for at least 15 minutes. The PA source was positioned on the same acoustic axis as the sensor at a distance of ~ 35 mm. The source was illuminated by the collimated output of the excitation laser via a multimode fiber. The pulse energy was attenuated to ~ 2 mJ and the spot size diameter measured ~ 2 mm.

We acquired PA image data sets for all samples in water (and without the samples as reference). The PA image volumes were reconstructed with the k-Wave toolbox [18] using a fast Fourier reconstruction algorithm [19] assuming a speed of sound of 1480 m s^{-1} .

3. Results and discussion

The printing parameters most effective in optimizing acoustic attenuation are the decrease in nozzle diameter to 0.2 mm, using a 0.1 mm layer height and the increase in porosity by using a 0.1 mm hole compensation – the parameters for the phantom marked as *final*. The measurements for the phantom can be seen in Figure 2, including the reference measurement through water, *ex vivo* human skull and two further phantoms.

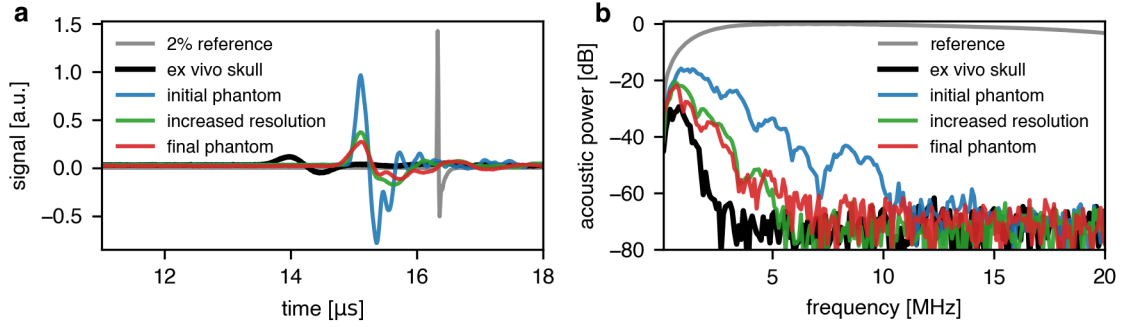


Fig. 2. **a** Representative PA waveforms measured in a single point of an FP sensor **b** Corresponding acoustic power spectra – discrete Fourier transforms of (a).

The measurements on *ex vivo* skull show large attenuation of signal components above ~ 2 MHz. The *initial phantom* did not match this attenuation, likely because the printing resolution (0.4 mm) was too low to accurately recreate the microstructure of the skull. Therefore, walls separating porous structures were not printed correctly, as these walls in the diploë are around 0.1 to 0.3 mm thick [11]. Increasing the printing resolution to 0.2 mm greatly improved the phantom's performance (*increased resolution* phantom). By increasing the porosity of the phantom artificially using the *x-y-hole compensation* the attenuation of the phantom was increased further. The *final* phantom printed with both increased resolution and improved porosity shows a reasonable match in acoustic attenuation compared to the *ex vivo* skull sample. Increasing the hole compensation even further led to merging pores and lower effective attenuation. Scaling up the phantom size (i.e. by 20 %), did not significantly change the acoustic attenuation. In initial tests, various infill patterns were evaluated, with no significant effect. The presented phantoms all use a rectilinear infill pattern and PLA Matte as the printing material.

Using the PA tomography setup, we also imaged the PA source through the *final* phantom and the *ex vivo* human skull. In Figure 3 maximum intensity projections (MIP) of an example image volume are shown (a-c) as well as example slices (d-f). A qualitative comparison of PA imaging through skull versus phantom shows a similar distortion and attenuation.

In conclusion: We presented a 3D-printed phantom which mimics *ex vivo* skull in both single point insertion loss measurements as well as in PAI. The phantom is easy to modify, adapt and fabricate as it is Open Data and made with widely available 3D printers and materials.

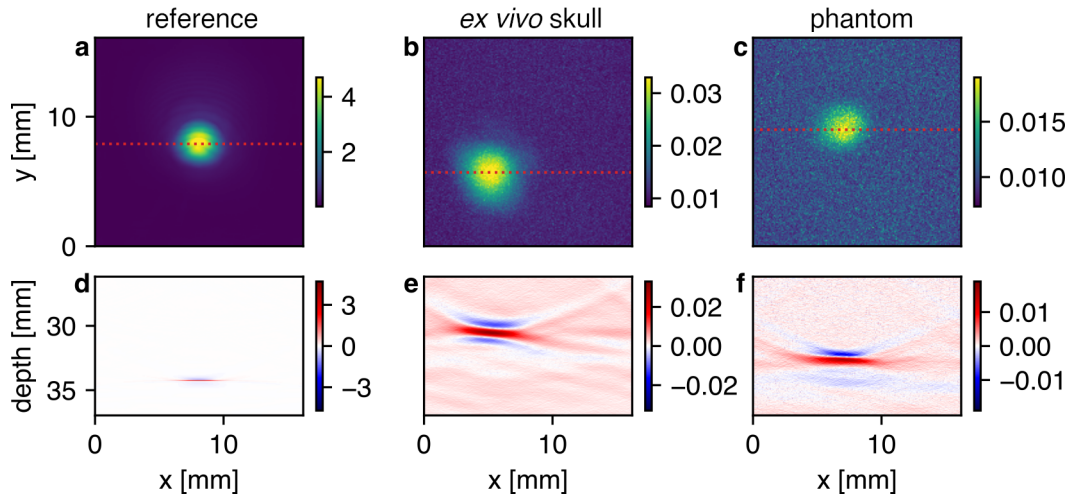


Fig. 3. PA imaging of a collimated laser spot projected onto a layer of black acrylic paint. **(a&d)** shows the reconstructed PA image through water with no skull, **(b&e)** through *ex vivo* frontal cranial bone and **(c&f)** through the *final* skull phantom. **(a-c)** maximum intensity projections (MIP) along the depth axis of the reconstructed PA images. **(d-f)** Selected longitudinal slices at the highlighted position (red dotted line in figures above). All figures are shown in a linear color scale.

Data availability

PAI volume data is available at doi:10.5281/zenodo.14876160, together with the 3D printable mesh files and parameters. The X-ray Micro-CT data set is Kirchner (2022) [10]. Data processing and analysis was primarily performed using the open-source k-Wave toolbox as described.

Acknowledgements

The authors would like to thank Heike Kielstein, Institute of Anatomy and Cell Biology, MLU Halle-Wittenberg for the provision of the human skull sample. This work was funded by the German Research Foundation (DFG, Deutsche Forschungsgemeinschaft) under grant number 471755457.

Credit authorship contribution statement

Hannah Linde: Data curation, Formal analysis, Investigation, Methodology, Validation, Visualization, Writing – original draft, Writing – review & editing. Saskia Menzer: Formal analysis, Investigation, Validation, Writing – review & editing. Jan Laufer: Methodology, Resources, Writing – review & editing. Thomas Kirchner: Conceptualization Funding acquisition, Methodology, Project administration, Software, Resources, Supervision, Validation, Visualization, Writing – original draft, Writing – review & editing.

References

1. J. Yao, L. V. Wang, Photoacoustic brain imaging: from microscopic to macroscopic scales, *Neurophotonics* 1 (1) (2014). doi:10.1117/1.NPh.1.1.011003.
2. Z. Wang, F. Yang, W. Shi, W. Xie, Z. Zhang, S. Yang, Monitoring the perivascular cerebrospinal fluid dynamics of the glymphatic pathway using co-localized photoacoustic microscopy, *Optics letters* 48 (9) (2023) 2265–2268. doi:10.1364/OL.486129.
3. C. Huang, L. Nie, R. W. Schoonover, Z. Guo, C. O. Schirra, M. A. Anastasio, L. V. Wang, Aberration correction for transcranial photoacoustic tomography of primates employing adjunct image data, *Journal of biomedical optics* 17 (6) (2012) 066016. doi:10.1117/1.JBO.17.6.066016.
4. B. Liang, S. Wang, F. Shen, Q. H. Liu, Y. Gong, J. Yao, Acoustic impact of the human skull on transcranial photoacoustic imaging, *Biomedical optics express* 12 (3) (2021) 1512–1528. doi:10.1364/BOE.420084.
5. S. Na, X. Yuan, L. Lin, J. Isla, D. Garrett, L. V. Wang, Transcranial photoacoustic computed tomography based on a layered back-projection method, *Photoacoustics* 20 (2020) 100213. doi:10.1016/j.pacs.2020.100213.
6. D. Leonov, M. Kodenko, D. Leichenko, A. Nasibullina, N. Kulberg, Design and validation of a phantom for transcranial ultrasonography, *International journal of computer assisted radiology and surgery* 17 (9) (2022) 1579–1588. doi:10.1007/s11548-022-02614-2.
7. T. Kirchner, C. Villringer, J. Laufer, Evaluation of ultrasound sensors for transcranial photoacoustic sensing and imaging, *Photoacoustics* 33 (2023) 100556. doi:10.1016/j.pacs.2023.100556.
8. Z. Xu, C. S. Locke, R. Morris, D. Jamison, K. M. Kozloff, X. Wang, Development of a semi-anthropomorphic photoacoustic calcaneus phantom based on nano computed tomography and stereolithography 3d printing, *Journal of orthopaedic research : official publication of the Orthopaedic Research Society* 42 (3) (2024) 647–660. doi:10.1002/jor.25702.
9. J. Poudel, S. Na, L. V. Wang, M. A. Anastasio, Iterative image reconstruction in transcranial photoacoustic tomography based on the elastic wave equation, *Physics in medicine and biology* 65 (5) (2020) 055009. doi:10.1088/1361-6560/ab6b46.
10. T. Kirchner, A micro-ct of a human skull (2022). doi:10.5281/zenodo.6108435. URL <https://zenodo.org/record/6108435>
11. S. L. Alexander, K. Rafaels, C. A. Gunnarsson, T. Weerasooriya, Structural analysis of the frontal and parietal bones of the human skull, *Journal of the mechanical behavior of biomedical materials* 90 (2019) 689–701. doi:10.1016/j.jmbbm.2018.10.035.
12. I. Wolf, M. Vetter, I. Wegner, T. Böttger, M. Nolden, M. Schöbinger, M. Hastenteufel, T. Kunert, H.-P. Meinzer, The medical imaging interaction toolkit, *Medical image analysis* 9 (6) (2005) 594–604. doi:10.1016/j.media.2005.04.005.
13. A. Auperrin, R. Delille, D. Lesueur, K. Bruyère, C. Masson, P. Drazétic, Geometrical and material parameters to assess the macroscopic mechanical behaviour of fresh cranial bone samples, *Journal of biomechanics* 47 (5) (2014) 1180–1185. doi:10.1016/j.jbiomech.2013.10.060.
14. J. C. Roberts, A. C. Merkle, C. M. Carneal, L. M. Voo, M. S. Johannes, J. M. Paulson, S. Tankard, O. M. Uy, Development of a human cranial bone surrogate for impact studies, *Frontiers in bioengineering and biotechnology* 1 (2013) 13. doi:10.3389/fbioe.2013.00013.
15. S. Pichardo, V. W. Sin, K. Hynynen, Multi-frequency characterization of the speed of sound and attenuation coefficient for longitudinal transmission of freshly excised human skulls, *Physics in medicine and biology* 56 (1) (2011) 219–250. doi:10.1088/0031-9155/56/1/014.

16. E. Zhang, J. Laufer, P. Beard, Backward-mode multiwavelength photoacoustic scanner using a planar fabry-perot polymer film ultrasound sensor for high-resolution three-dimensional imaging of biological tissues, *Applied optics* 47 (4) (2008) 561–577. doi:10.1364/ao.47.000561.
17. J. Buchmann, J. Guggenheim, E. Zhang, C. Scharfenorth, B. Spannekrebs, C. Villringer, J. Laufer, Characterization and modeling of fabry-perot ultrasound sensors with hard dielectric mirrors for photoacoustic imaging, *Applied optics* 56 (17) (2017) 5039–5046. doi:10.1364/AO.56.005039.
18. B. E. Treeby, B. T. Cox, k-wave: Matlab toolbox for the simulation and reconstruction of photoacoustic wave fields, *Journal of biomedical optics* 15 (2) (2010) 021314. doi:10.1117/1.3360308.
19. K. P. Köstli, M. Frenz, H. Bebie, H. P. Weber, Temporal backward projection of photoacoustic pressure transients using fourier transform methods, *Physics in medicine and biology* 46 (7) (2001) 1863–1872. doi:10.1088/0031-9155/46/7/309.